Computer simulation of disordering and premelting of low-index faces of copper

H. Häkkinen and M. Manninen
Department of Physics, University of Jyväskylä, SF-40351 Jyväskylä, Finland
(Received 9 September 1991; revised manuscript received 16 March 1992)

Molecular dynamics and the effective-medium theory have been applied to investigate the structure and dynamics of (110), (100), and (111) faces of copper in the whole temperature range from 0 K up to the bulk melting point, which has been determined to be 1240±25 K. The observed order in the surface stability follows the order in the packing density. (110) disorders first via anharmonic effects (up to 700 K), then by vacancy-adatom formation and finally by premelting of the surface at about 1200 K. The (110) solid-melt interface is anisotropic and broadened, having a tendency to form small fluctuating (111) facets in equilibrium, which is suggested to be the atomic-scale melting mechanism in that direction. On the contrary, (111) is very stable up to the bulk melting point and even shows weak superheating effects. Premelting is also lacking on (100). The melting proceeds in these directions by a layer-by-layer mechanism. These observations correlate both with the experimental findings and with the thermodynamic models of the surface stability of fcc metals.

I. INTRODUCTION

A lot of recent theoretical and experimental work has been devoted to the understanding of the surface *premelting* property of crystalline materials, i.e., the situation where *in equilibrium* the surface of the crystal is covered by a thin liquidlike film below the thermodynamical bulk melting point T_m^1. While the original idea of surface-initiated crystal melting is very old,[2,3] direct measurements on clean single-crystal surfaces have been possible only during the past decade.[4–13] Another type of disorder, called *roughening,* is also proposed to occur on several loose-packed crystal surfaces.[14,15] On the atomically rough surface, atoms still occupy the crystalline positions, while the premelted surface has liquidlike structural, mechanical, and transport properties. However, the surface-liquid film is affected by the underlying solid substrate, which is the reason why it is often called *quasiliquid.*

Thermodynamically, roughening involves the disappearance of the free energy of formation of an atomic step or kink on the surface, while the thermodynamical condition for premelting of a crystal face (hkl) can be expressed by means of the interfacial free energies per unit area

$$\gamma_{\mathrm{SV}}^{(hkl)} > \gamma_{\mathrm{SL}}^{(hkl)} + \gamma_{\mathrm{LV}} , \tag{1}$$

where the free energies are those for solid-vapor (SV), solid-liquid (SL), and liquid-vapor (LV) interfaces, respectively. However, both roughening and premelting can occur on the same surface, roughening being a precursor state for premelting. The Miller indices (hkl) have been explicitly added to Eq. (1) as a reminder that the crystal-face anisotropy can strongly affect the tendency to premelt.[16]

A theoretical approach to surface-initiated melting may involve thermodynamical models based on Landau free-energy functional[17–19] lattice-instability models,[20–22] or computer simulations.[23–33] Models based on Landau theory lead to a consistent qualitative description of premelting with respect to experiments, predicting, e.g., the divergence of the quasiliquid thickness as a function of the reduced temperature, $\ln(T-T_m)$ or $(T-T_m)^r$, depending on whether the atomic interactions are short ranged or long ranged, respectively. For a microscopic (atomic-scale) description of disordering and surface-initiated melting, relaxations, reconstructions, and crystallographic surface anisotropy should be taken into account. Lattice-instability models have demonstrated clearly the stabilizing role of surface relaxation against disordering and melting, but they have failed, e.g., in predicting that the relaxed Cu(110) face should be more stable than the relaxed Cu(111) face,[22] contrary to experiments.[4–6] It is clear that the more realistic microscopic description of disordering and premelting phenomena on crystal surfaces can be obtained using computer-simulation methods, especially the molecular-dynamics (MD) method, where the real dynamics of the atomic system can be followed. Unfortunately, while MD simulations have been successful in describing disordering and premelting of low-index faces of rare-gas (Lennard-Jones) solids,[23–25] realistic interatomic potentials for metallic systems have been available only during the past few years.[34] Up to now, MD simulations with these models have been made on Al(110) (Ref. 29) using the effective-medium theory,[35] on Ni(110),[30] and Cu(110) (Ref. 32) using the embedded-atom method (EAM) (Ref. 36), and on Au(111) using the "glue model."[31] A premelting phenomenon driven by the vacancy-adatom mechanism has been observed in simulations on all the studied (110) surfaces. Au(111), on the other hand, seems to be quite stable against surface melting due to the high packing density. We are not aware of MD simulations on any fcc(100) metal surface, which is experimentally seen to preserve its crystalline structure very close to the bulk melting point.[4–6]

The purpose of the present work is to make a contribu-

tion to our understanding of the atomic-scale mechanisms underlying the experimentally observed disordering and premelting phenomena on metal surfaces. We have studied the structure and dynamics of (110), (100), and (111) faces of copper in the whole temperature range from 0 K up to the melting point using the molecular-dynamics method together with the effective-medium theory (EMT).[35] While previous simulations of metals applying realistic many-atom potentials have usually concentrated only on the (110) face, this work studies *all* the low-index faces of a fcc metal, using the same interatomic potential and comparable sample sizes. This allows us to directly compare the behavior of the different crystal faces, which generally is quite difficult between different simulations due to the variations in potentials and to different finite-size effects.

The main results of this work are summarized as follows: The order in the surface stability against disordering and melting follows the order in the packing density, i.e., the most open (110) face disorders at the lowest temperature and the close-packed (111) face is the most stable one. On (110), the disordering starts by anharmonic effects, which result in vacancy-adatom formation beyond 700 K and finally in premelting of the surface at about 1200 K. The thermodynamic melting point of bulk copper in EMT is determined to be 1240±25 K. On (100), disorder is found only for the first crystal layer near T_m. (111) is stable against premelting and shows weak superheating effects. The (110) solid-melt interface is anisotropic and broadened, having a tendency to form small (111) facets in equilibrium. This faceting mechanism is proposed to be the leading atomic-scale melting mechanism in fcc metals, as compared to the more layer-by-layer mechanism in the [100] and [111] directions.

We continue by describing briefly our method of simulation and the model potential in Sec. II. Section III discusses the surface energies and the relaxation at zero temperature of (110), (100), and (111) faces. The estimation of the thermodynamic melting point of copper in EMT is discussed in Sec. IV. The anharmonic properties (lattice vibrations, thermal expansion) of the different faces are compared in Sec. V, and the disordering and premelting phenomena are compared in Sec. VI. Finally, the conclusions of this work are given in Sec. VII.

II. MODEL AND METHOD

All the calculations have been made with the usual slab geometry, where periodic boundary conditions are imposed in the x-y plane and the surface under investigation is perpendicular to the free z direction. Atoms in four layers on one side of the slab are held fixed in their crystallographic positions to mimic the underlying solid substrate. The thickness of the fixed area is more than the range of interatomic potential, which means that the atoms moving near the static layers do not see the static surface. The lattice parameter of the sample is set to correspond to the simulated temperature according to the independently simulated zero-pressure thermal-expansion curve for bulk copper.[37] The number of dynamic layers N_z and atoms in each layer N_{xy} are tabulated in Table I, together with the crystallographic orientations of the x, y, and z directions on each face. In the ($T=0$) surface energy and relaxation calculations, we have used a slab having approximately 500 dynamical atoms, whereas in the disordering and premelting simulations the size of the sample has been approximately 2000 dynamical atoms. Compared to the previous simulations of premelting of metals,[29–32] our sample sizes are quite big. We have made preliminary simulations of Cu(110) using a slab with two free surfaces and with approximately twice as many dynamical layers in the z direction and half of the number of atoms in each layer as compared to values given in Table I. However, for practical reasons in analysis, we chose the slab with only one free surface for the systematic study. We have verified that both simulation geometries result in the same picture for disordering and premelting of Cu(110). We therefore expect that there are no significant finite-size effects in our results, especially when comparing the behavior of (110), (100), and (111) faces, since we have used similar sample sizes for all these faces.

We have carried out three different types of MD simulations: dynamical quenching to find out the relaxed zero-temperature structure of the surface, constant-temperature (canonical) simulations to determine the thermodynamical bulk melting point of copper in our model, and combined constant-temperature and constant-energy (microcanonical) simulations to study the disordering and premelting phenomena. The quenching procedure was started from the unrelaxed (bulk-terminated) positions of atoms on the surface. While doing ordinary MD, the signs of the products of the velocity and force components for each atom, $v_{i\alpha}F_{i\alpha}$ ($\alpha=x,y,z$) were checked at each time step. Whenever any of these products was negative, meaning that an atom i was moving out of a local energy minimum, the velocity component in that direction was set to zero. This procedure

TABLE I. Characteristics of the calculational box used for the (110), (100), and (111) faces in simulation of surface disordering and melting. N_z is the number of dynamic layers and N_{xy} is the number of atoms in a layer. $N_{\text{tot}}=N_zN_{xy}$. The numbers in parentheses are those used in the zero-temperature calculations. Also shown are the crystallographic orientations of the x, y, and z edges of the simulation box.

(hkl)	x	y	z	N_z	N_{xy}	N_{tot}
(110)	⟨100⟩	⟨110⟩	⟨110⟩	26(10)	88(48)	2288(480)
(100)	⟨100⟩	⟨100⟩	⟨100⟩	20(10)	98(50)	1960(500)
(111)	⟨110⟩	⟨112⟩	⟨111⟩	20(8)	90(56)	1800(448)

was able to rapidly quench the system into the relaxed zero-temperature structure, from which the surface energy and the magnitude of the surface relaxation were determined. To determine the thermodynamical bulk melting point of copper, a method capable of supplying latent heat was needed. We used the Nosé-Hoover thermostat,[38] where the system is coupled with an external heat bath by an extra degree of freedom. Overall, in this work we have used the velocity-Verlet algorithm[39] to integrate the equations of motion. Modification of that algorithm to include the Nosé-Hoover thermostat is discussed in Appendix A.

The simulation runs for disordering and premelting consisted of a stochastic equilibration period of 1000–2000 time steps (14–28 ps), followed by a constant-energy period of 2000 time steps, during which the structural data were produced for the analysis. The stochastic equilibration was carried out by choosing randomly at time intervals of 1–100 time steps the velocities of all atoms from the Maxwell-Boltzmann distribution corresponding to the desired temperature. This procedure was able to remove strong correlated collective motion of atomic layers parallel to the free surface, which is a well-known artifact of the slab geometry.[24] The collective motion of the layers is connected with their initial nonzero center-of-mass velocities (although the center-of-mass velocity for the whole sample is initially set at zero) and is very weakly damped in normal MD, especially at low temperatures, and for the (111) layers, which are the easy-glide layers in the fcc structure. The stochastic equilibration can therefore be viewed as a way to accelerate the energy dispersion from these initially generated vibrational modes to other modes in the system.

The trajectories for data analysis were produced by using the microcanonical MD, primarily because the rms fluctuations in the total energy provide a direct measure for the numerical accuracy of the simulation (see Appendix A), and because the fluctuations in temperature are also somewhat smaller than in canonical methods. The energy and structural quantities of each layer were monitored continuously during the simulation, and equilibrium was interpreted to be achieved when there were no significant temporal variations in the energy, occupation, order parameter, or diffusion constant of each layer and the magnitude of the rms fluctuations were in accordance with the statistical expectations. Near melting, a whole sequence of equilibration and production phases was repeated to check that the system was in equilibrium. The longest simulation time at a given temperature has been of the order of 100 ps. The temperature was raised by steps of 50–100 K and the last configuration at the previous temperature was used as the initial configuration for the next temperature, with an appropriate scaling of the lattice parameter. The thermal averages have been calculated typically over 200 configurations, separated by ten time steps (0.14 ps), which we concluded is sufficient to make the collected configurations statistically uncorrelated.

The interactions between copper atoms are described by the effective-medium theory,[35] which is an approximate method of calculating the total energy of an arbitrary arrangement of metal atoms from their spatial positions. EMT has been shown to be a powerful scheme to describe the number of bulk and surface properties of metals, such as thermal expansion and bulk melting,[37,40] defect energies,[41] dislocations,[42] surface relaxation and reconstructions,[43,44] high-temperature dynamics of a surface,[29] and also properties of metal-impurity systems[45] and small clusters.[46] The many-atom nature of metallic cohesion is crucial in most of these problems, which is the point where EMT has a clear advantage over the classical pair potentials. Compared to the other many-atom potentials for metals, EMT has the strongest *ab initio* nature, since, in principle, *all* the parameters needed in the total-energy expression can be *calculated* using the jellium model and the density-functional theory with the local-density approximation.[47] Other models, while resulting in a similar functional form for the total energy, are usually constructed in a more empirical way.

The original EMT formalism was constructed for a fcc lattice with only nearest-neighbor interactions.[35] In this work, the cutoff range of the interactions is between the third- and the fourth-nearest neighbors in the zero-temperature copper lattice. We decided to use this longer cutoff because of our previous results at high temperatures and in disordered phases.[37] We employ the "shifted-force" cutoff, where the potential and the force go smoothly to zero at cutoff. Our present method is a direct generalization of our previous extension of the atomic interactions beyond the nearest neighbors in bulk calculations[37] to systems having a crystal surface. Since our method deviates slightly from the procedure described in Refs. 29 and 35, a brief discussion of the technical details is given in Appendix B.

III. ZERO-TEMPERATURE CALCULATIONS

After quenching the system to the relaxed zero-temperature state as described in Sec. II, the atomic-sphere radius (see discussion of EMT in Appendix B), total energy per atom, changes in layer spacings, and surface energy were calculated for the surface region of all the low-index faces. At zero temperature, the atomic-sphere radius s in EMT coincides with the definition of the Wigner-Seitz radius. s is then a measure of the local electron density. As seen in Table II, s is largest on (110), since the loosest packing of atoms is on that face; correspondingly, the close-packed (111) has the smallest s. The bulk value $s_0 = 2.5776 a_0$ is reached in layer 5 of (110) and in layer 4 of (100) and (111). This shows the range of the surface effects into the bulk. The total energy per atom for different layers given in Table II shows similar convergence to the bulk value $E_0 = -3.56$ eV, which is (negative of) the cohesive energy of copper in our model. It is interesting to note that layer 3 of (110) and layer 2 of (100) and (111) have a slightly greater electron density than the bulk layers. There is also a weak oscillation in the total energy before the bulk energy is approached on all these faces.

Table III shows the relaxation, i.e., the change of surface-layer spacing from the bulk value, for all the faces

TABLE II. The relaxed $T=0$ values for the Wigner-Seitz radius s (a_0) and the total energy E (eV) for the first five layers of the (110), (100), and (111) faces of copper calculated from EMT.

(*hkl*)	*l*	s (a_0)	E (eV)
(110)	1	2.7457	−2.9502
	2	2.6016	−3.4107
	3	2.5726	−3.5557
	4	2.5771	−3.5610
	5	2.5776	−3.5602
(100)	1	2.7118	−3.0918
	2	2.5743	−3.5333
	3	2.5771	−3.5612
	4	2.5776	−3.5601
	5	2.5776	−3.5600
(111)	1	2.6740	−3.1733
	2	2.5724	−3.5556
	3	2.5777	−3.5605
	4	2.5776	−3.5600
	5	2.5776	−3.5600

studied. EMT leads to contraction of the uppermost layer spacing on all the faces studied, the inward relaxation being largest on (110). Table III also shows results from two other many-atom models, EAM,[36] and the model by Ackland, Tichy, Vitek, and Finnis (ATVF).[48] All these models give quite similar *inward* relaxation. This is one point where many-atom models are more realistic than the classical pair potentials, which generally predict *outward* relaxation[49] contrary to experiments. In this work, small relaxation is seen on (110) up to d_{56}, the whole sequence being (not shown in Table III) −3.7%, −0.1%, −0.3%, +0.2%, −0.1%, and 0.0% for d_{12}, d_{23}, d_{34}, d_{45}, d_{56}, and d_{67}, respectively. This multilayer, weakly oscillatory behavior is qualitatively similar to that observed in experiments[50,51] and also in the pseudopotential calculations,[52] although differences exist in the magnitude of the relaxation. In EMT, the driving force of relaxation is the gain in "embedding energy" E_C (Appendix B) due to the increase in the local electron density of the surface layer. On the other hand, the opposing force comes from the atomic-sphere correction term E_{AS}. For a detailed discussion of the physics involved in the surface relaxation in EMT we refer to Refs. 35 and 53.

TABLE III. The relaxation of the two uppermost layer spacings d_{12} and d_{23} calculated at $T=0$ from EMT. For comparison, values obtained from EAM (Ref. 36) and the ATVF model (Ref. 48), together with the experimental results of low-energy electron diffraction (LEED) (Ref. 50) and medium-energy ion scattering (MEIS) (Ref. 51) are given for the (110), (100), and (111) faces of copper. Also shown are the calculated values for the surface energy E_s. Relaxations are defined as a percentage change of the lattice spacing from the bulk value and surface energies are in ergs cm^{-2}.

Face	Method	d_{12} (%)	d_{23} (%)	E_s (ergs cm^{-2})
(110)	EMT	−3.7	−0.1	1416
	EAM	−3.0	0.0	1400
	ATVF	−4.5	−0.5	1233
	LEED	−8.5	+2.3	
	MEIS	−5.3	+3.3	
(100)	EMT	−1.0	−0.1	1296
	EAM	−1.2	0.0	1280
	ATVF	−1.3	−0.1	1144
(111)	EMT	−1.2	0.0	1185
	EAM	−1.4	0.0	1170
	ATVF	−1.8	+0.1	947
	LEED	−0.7		

We did not observe any reconstruction effects, i.e., intralayer structural changes in the surface region, on any of the studied faces. We have previously shown[44] that, e.g., the (1×2) missing-row reconstruction is not favored at zero temperature on clean Cu(110) in EMT.

The last column in Table III shows the calculated surface energies for different faces compared to the results from the EAM and ATVF models. It is seen that all these models give comparable surface energies, which are clearly smaller than the experimental estimate for the surface energy of copper, 1790 ergs cm^{-2} by Tyson and Miller.[54] However, the calculated values are quite reasonable, since the experimental estimate is an average over a large number of different crystal faces, including many high-energy loose-packed faces, also. It is worth noting that the surface energies of copper given by EMT and EAM are very close to each other. As discussed in Sec. VII, these two models lead to quantitatively comparable descriptions of the premelting of Cu(110).

IV. THERMODYNAMICAL MELTING POINT

In order to decide whether the observed melting of the surface is indeed *premelting*, i.e., occurs at $T \leq T_m$, we must find an estimate for the thermodynamical melting point T_m of our model. At least three methods for estimating the melting point have been given in the literature. The most elegant and thermodynamically valid method is based on the calculation of the Gibbs free energies of the bulk solid and the liquid phases as functions of temperature. T_m is then found, by definition, by making the free energies of solid and liquid equal.[55] However, this method is computationally quite elaborate and contains a fairly large source of inaccuracy, due to the fact that the free energies usually depend quite weakly on temperature, and T_m is then an intersection point of two flat curves. In the second method, one tries to determine the temperature-dependent velocity of the moving solid-liquid interface v_{SL} at $T > T_m$ and thus, by extrapolating to zero velocity, one can find the solid-liquid coexistence point, which is interpreted to be T_m. This method has been shown to give a melting point comparable to what is obtained from the thermodynamic method when applied to the Stillinger-Weber potential (silicon) and to EAM (copper).[55] The third method is computationally the most straightforward one. In this method, an excess amount of kinetic energy is given to the surface region of the sample, which results in a temperature gradient and

nucleates melting. Heating is then stopped and the sample is allowed to evolve to equilibrium, and the solid-liquid coexistence temperature is interpreted as T_m.[56] All these methods are able to give an estimate for T_m with comparable accuracy, and at present it is not possible to set a method preferable to any other.

We have used the second method and determined v_{SL} at six temperatures in the range of 1300–1600 K in a slab with one free (110) surface. The (110) slab was chosen in these calculations because it had been found to have a dominant role in nucleating melting transition among the faces studied. Melting in the [100] and [111] directions is expected to proceed by a more layer-by-layer mechanism than in the [110] direction, which may give rise to weak superheating effects on the solid-liquid interface at temperatures just above T_m and makes a reliable estimation of v_{SL} more difficult. We started with a sample having a few liquidlike layers on the surface and applied the Nosé-Hoover thermostat to supply latent heat into the system. At each temperature the system was followed until the solid-liquid interface had moved near the static substrate. The velocity of the solid-liquid interface was determined from the linear rise in the total energy of the system during melting. The estimated v_{SL}'s at different temperatures are plotted in Fig. 1. By using a quadratic fit the velocity is found to go to zero at 1240±25 K, which is then interpreted as the thermodynamical melting point of copper in our model potential. This agrees reasonably well with the experimental triple point of 1356 K,[57] especially when one bears in mind the *ab initio* nature of the potential parameters.

Finally, we want to point out that in bulk simulations (employing periodic-boundary conditions in three dimensions) starting from the ordered lattice, melting is observed to take place beyond 1500 K for copper in EMT.[37] This transition temperature is not the true thermodynamical T_m, but the mechanical instability point which satisfies the Born criterion for crystal melting.[58] This shows that the superheating region in MD calculations for metals may be as large as 250 K or more (20% of T_m of Cu) and great care should therefore be exercised while determining T_m from simulation results.

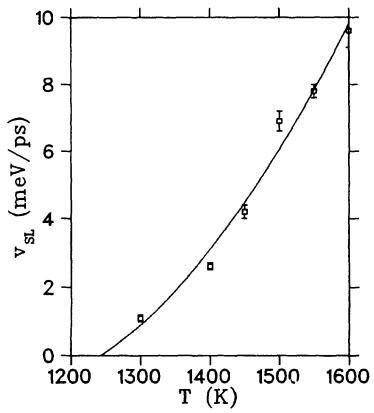

FIG. 1. The velocity of the (110) solid-liquid interface v_{SL} as a function of temperature. The estimated solid-liquid coexistence point is 1240±25 K.

V. SURFACE ANHARMONICITY

The vibrational properties of the (110) and (100) faces of copper have attracted continuous experimental interest during recent years.[59–64] The strong anharmonicity of these faces is also the key to understanding the production of vacancies and adatoms at high temperatures, which eventually can lead to roughening or premelting transitions (or both). The anharmonicity manifests itself as a larger thermal-expansion coefficient of the surface area and also as an anomalous increase in the vibrational amplitudes of the surface atoms. In this section we compare the surface anharmonicities of the (110), (100), and (111) faces by discussing the relaxation of surface layers and the vibrational amplitudes of surface atoms at temperatures below 1000 K.

We show in Fig. 2 the calculated relaxation d_{12} for these faces as a function of temperature, defined as the percentage change of the layer spacing with respect to the value corresponding to the bulk lattice parameter at the temperature in question. If the thermal-expansion coefficient of the surface region were the same as that of the bulk, the relaxation curve $d_{12}(T)$ would be a horizontal line. The rising curves in Fig. 2 show the enhanced anharmonicity of the surface on each of the faces studied. The thermal expansion is quite comparable on (110) and (100), on which it is clearly larger than on (111). Notice that our calculation of $d_{12}(T)$ on Cu(110) involves only atoms on the first and second crystal layers. It does not contain the contribution of adatoms (which are handled as a distinct layer throughout our analysis), which are formed beyond 700 K. If adatoms would be included, the $d_{12}(T)$ curve would rise strongly in the range 700–1000 K.

We define the time-dependent mean-squared displacement (MSD) for the surface layers as

$$[\Delta \mathbf{r}(t)]_l^2 = \frac{1}{N_\tau N_l} \sum_{i=1}^{N_\tau} \sum_{j=1}^{N_l} [\mathbf{r}_j(t+\tau_i) - \mathbf{r}_j(\tau_i)]^2 , \qquad (2)$$

where $\mathbf{r}_j$ is the time-dependent position vector of atom j,

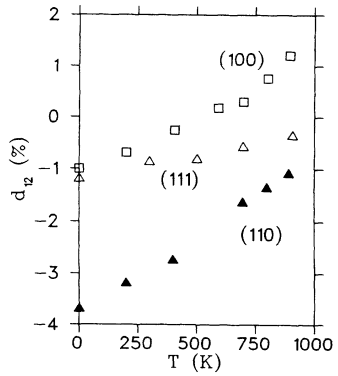

FIG. 2. The relaxation of the uppermost interlayer spacing d_{12} as a function of temperature for (110), (100), and (111).

N_l is the instantaneous number of atoms in layer l, and N_τ is the number of time origins, which is used to improve statistics. We want to stress here that the time average $\langle[\Delta\mathbf{r}(t)]_l^2\rangle$ does not coincide with that of the mean-square *deviation,* usually denoted by $\langle u^2\rangle$, where the reference system is the ideal lattice. This is simply because the position vectors at different time origins $\mathbf{r}(\tau_i)$ already include displacements from the ideal lattice positions. In fact, if the ideal lattice positions $\mathbf{r}_0$ were taken as reference points, our calculated $\langle[\Delta\mathbf{r}(t)]^2\rangle$ would be

$$\begin{aligned}\langle[\Delta\mathbf{r}(t)]^2\rangle &= \langle\{[\mathbf{r}(t+\tau)-\mathbf{r}_0]-[\mathbf{r}(\tau)-\mathbf{r}_0]\}^2\rangle \\ &= \langle[\mathbf{r}(t+\tau)-\mathbf{r}_0]^2\rangle + \langle[\mathbf{r}(\tau)-\mathbf{r}_0]^2\rangle \\ &\quad -2\langle[\mathbf{r}(t+\tau)-\mathbf{r}_0][\mathbf{r}(\tau)-\mathbf{r}_0]\rangle \\ &= 2\times\langle u^2\rangle\ , \end{aligned} \tag{3}$$

because we assume the displacements related to different time origins to be uncorrelated and, therefore, the cross term

$$\langle[\mathbf{r}(t+\tau)-\mathbf{r}_0][\mathbf{r}(\tau)-\mathbf{r}_0]\rangle$$

in Eq. (3) vanishes. In order to simplify the notation, we hereafter denote our calculated MSD by u^2 and take into account the factor 2 when comparing with the experimental MSD values.

In Fig. 3 we have plotted the z component (perpendicular to the surface) of the calculated mean-squared vibrational amplitude $\langle u^2\rangle$ as a function of temperature for surface layers of (110), (100), and (111), together with the experimentally determined $\langle u_z^2\rangle(T)$ on Cu(110) and Cu(100).[62] Figure 3 also includes the measured $\langle u_x^2\rangle(T)$ for bulk copper.[65] It is seen in Fig. 3 that EMT describes extremely well the anharmonicity of bulk copper, the measured and calculated MSD falling on the same curve. The largest discrepancy is near $T=0$, since MD cannot describe the quantum-mechanical zero-point motion. We have previously shown[37] that the thermal expansion of bulk copper in EMT closely follows the experiments, which is also a sign of realistic description of the anharmonic part in the interactions between copper atoms in the bulk. The same excellent agreement also holds between the calculated and measured perpendicular MSD's on the (100) face. On (110), the calculated MSD values for the first layer follow closely the measured curve below 500 K. At higher temperatures the well-known anomalous increase in the measured perpendicular surface fluctuations takes place.[62,63] A similar increase around 700 K would be obtained from our calculations if the contribution of adatoms were taken into account in layer 1. The (110) face is also anomalous in the sense that the calculated MSD for the *second* layer is equal to that for the first layer up to 700 K. It is clear that the experimentally determined perpendicular MSD does not directly correspond to our result, which has been calculated for each layer separately, since the diffracted helium[62] or neon[63] atoms measure perpendicular fluctuations in the average electron density profile, which is affected at high temperatures by atoms belonging to *three* layers (partial layer of adatoms and the two uppermost crystal layers). It is interesting that the temperature behavior of the calculated z component of MSD in the first layer on (111) is very similar to that in the (110) and (100) surface layers. The potential that the surface atoms feel perpendicular to the surface is therefore much the same on all low-index faces.

On the other hand, significant differences between faces exist in the vibrations parallel to the surface. Figure 4 shows the calculated in-plane MSD values for each face. It can be seen that on (110) the atoms vibrate perpendicular the nearest-neighbor chains (x direction) with larger amplitude than in the direction of the chain. The vibra-

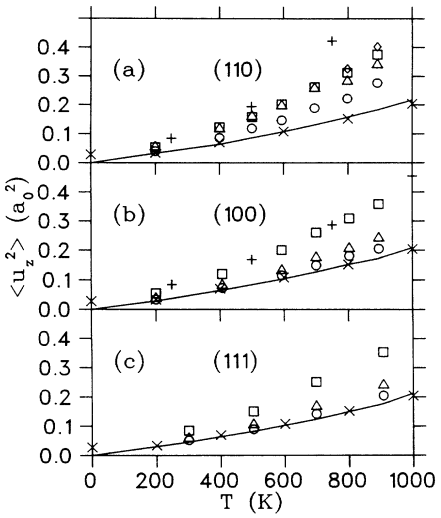

FIG. 3. The calculated perpendicular component of the mean-squared vibrational amplitude $\langle u_z^2\rangle$ as a function of temperature for different layers l of (a), (110), (b) (100), and (c) (111). Diamonds, $l=0$ (adatoms); squares, $l=1$; triangles, $l=2$; circles, $l=3$; solid line, $l=10$ (bulk). The pluses are the experimentally measured $\langle u_z^2\rangle$ for the (110) and (100) face (Ref. 62) and the crosses are the experimental $\langle u_x^2\rangle$ for the bulk copper (Ref. 65). The experimental values have been multiplied by a factor of 2 to remove the discrepancy between the ways to define MSD, as discussed in the text.

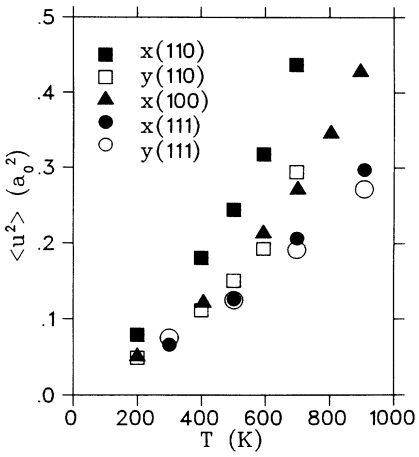

FIG. 4. The calculated in-plane components of MSD as a function of temperature for the surface layer of (110), (100), and (111).

tion amplitudes on (100) (where x and y are identical directions) are about the same as in the chain direction on (110). On (111), the amplitudes are smallest and nearly isotropic in the x and y directions ($\langle 110 \rangle$ and $\langle 112 \rangle$, respectively). By comparing Figs. 3 and 4, it can be seen that for surface atoms on (110), the in-plane vibrations are larger than the out-of-plane vibrations; on (100), atoms vibrate with comparable amplitudes in both the in-plane and out-of-plane directions; and on (111), the in-plane vibrations are somewhat smaller than the out-of-plane vibrations. These results reflect the crystallographic fact that in the loose-packed crystal layers, atoms are more tightly bound with atoms in the adjacent layers than with their in-plane neighbors, whereas the close-packed crystal layers have relatively weak "bonds" with the adjacent layers.

The Lindeman rule of melting[66] states that melting should take place when the amplitude of the root-mean-squared vibrations exceeds in some direction a certain fraction (about 10%) of the distance between the nearest neighbors. When applied to our calculated MSD values (remembering the factor of 2), the critical MSD value obtained by the Lindeman rule falls in the range 0.4–0.5 a_0^2. This criterion is fulfilled by the in-plane vibrations of surface atoms well below 1000 K on both (110) and (100), while both surfaces still clearly preserve their crystalline state. The Lindeman rule fails for the surface-initiated melting becauses it relates the vibrations to the *bulk* anharmonicity[67] and cannot account for the enhanced anharmonicity of a surface. We have verified that the Lindeman rule indeed applies much better to the melting in the bulk, the one-dimensional rms vibrational amplitude for the bulk and solid layers being about 10% of the nearest-neighbor distance around 1250 K, which is essentially the same temperature as our estimated T_m.

The MD method may include two artifacts that must be taken into account in interpreting our MSD results. The finite size of our sample may generate collective motion in the close-packed directions, e.g., in the direction of the nearest-neighbor chains on (110), which leads to overestimation of the MSD values in that direction. However, this effect can be expected to be the strongest in samples with sizes smaller than those used in this work. Furthermore, the stochastic thermalization reduces the generation of the collective vibrational modes. On the other hand, our calculated MSD values are systematically underestimated, since we have not extrapolated the results to the thermodynamical limit (infinite sample). With the sample sizes used in this work, we expect this effect to be below 10%.[68]

VI. DISORDERING AND PREMELTING

A. Structure factors

For studying the translational order of surface layers during the disordering process, we have calculated the in-plane structure factor, defined as

$$S_l(\mathbf{k}) = \frac{1}{N_l} \sum_{j=1}^{N_l} e^{i\mathbf{k}\cdot\mathbf{r}_j} , \tag{4}$$

where $\mathbf{k}$ is the reciprocal-lattice vector parallel to the surface and the sum runs over the position vectors of atoms $\mathbf{r}_j$ (N_l in total), which belong to layer l. The thermal average of the magnitude squared of the structure factor, $\langle |S_l(\mathbf{k})|^2 \rangle$, is usually used as an order parameter, being one for an ordered layer at $T=0$ K and near zero for a disordered layer. However, this order parameter has the drawback that it is not sensitive to the nature of the disorder but, in addition to the premelting, lattice vibrations and vacancy formation also make it decrease from unity. The effect of harmonic lattice vibrations can be accounted for by a Debye-Waller factor,[67] which produces a linear decrease of $\ln\langle |S_l(\mathbf{k})|^2 \rangle$ as a function of temperature. We shall show that anharmonic effects can also be filtered out from the order parameter. To this end we shall make use of the fact that our calculated mean-square displacements $\langle u^2 \rangle$ contain at lower temperatures (below the onset of vacancy-adatom formation) information regarding the surface anharmonicity. The calculated order parameter can then be corrected by an "anharmonic" or a "quasiharmonic" Debye-Waller factor

$$|S_l^{\mathrm{corr}}(\mathbf{k},T)|^2 = e^{\frac{1}{2}k^2\langle u_{\mathbf{k}}^2(T)\rangle} |S_l^{\mathrm{calc}}(\mathbf{k},T)|^2 , \tag{5}$$

where $\langle u_{\mathbf{k}}^2(T) \rangle$ is a quadratic fit to our calculated MSD values in the direction of $\mathbf{k}$ and the factor $\frac{1}{2}$ arises from

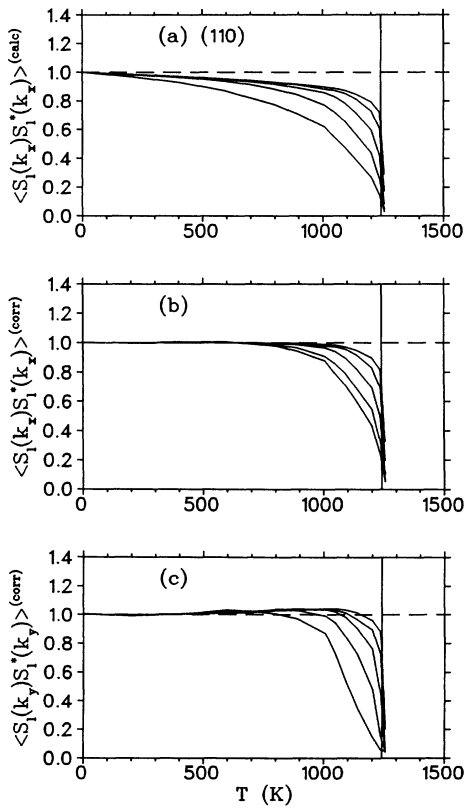

FIG. 5. The order parameter $\langle |S_l(\mathbf{k})|^2 \rangle$ as a function of temperature for the first five crystal layers of (110). (a) Calculated and (b) corrected values for $\mathbf{k}=(2\pi/a)(1,0)$, (c) corrected values of $\mathbf{k}=(2\sqrt{2}\pi/a)(0,1)$. The lowest curves in (a)–(c) for $l=1$ and the uppermost curves are for $l=5$. The vertical line shows the estimated thermodynamical melting point T_m.

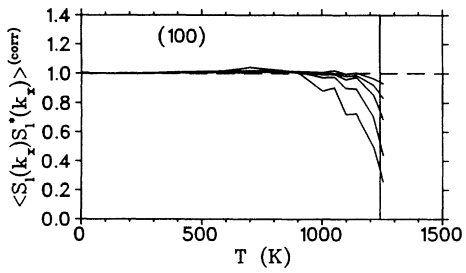

FIG. 6. The corrected order parameter $\langle |S_l(\mathbf{k})|^2 \rangle$ as a function of temperature for the first five crystal layers of (100) for $\mathbf{k}=(4\pi/a)(1,0)$.

our definition of MSD as discussed in Sec. V.

The calculated and corrected order parameters for surface layers are shown as a function of temperature in Figs. 5–7 for (110), (100), and (111), respectively. The reciprocal-lattice vectors that have been used are $\mathbf{k}_x=(2\pi/a)(1,0)$ and $\mathbf{k}_y=\sqrt{2}|\mathbf{k}_x|(0,1)$ for (110), $\mathbf{k}_x=(4\pi/a)(1,0)$ and $\mathbf{k}_y=|\mathbf{k}_x|(0,1)$ for (100), and $\mathbf{k}_x=(4\sqrt{2}\pi/a)(1,0)$ and $\mathbf{k}_y=(1/\sqrt{3})|\mathbf{k}_x|(0,1)$ for (111). We find that the corrected order parameters for the first crystal layers of (110), (100), and (111) remain practically unity up to 700, 900, and 1100 K, respectively. These temperatures correspond to the onset of vacancy-adatom formation on each of these faces, as will be discussed in Sec. VI B. The effects of harmonic and anharmonic lattice vibrations are then filtered out from the order parameter. Notice that the existence of vacancies does not directly affect the order parameter, since normalization is made at each time step by using the instantaneous layer occupation N_l in Eq. (4). Vacancies have an indirect effect by inducing distortions in the surface region, as can be seen from the snapshots shown in Sec. VI E.

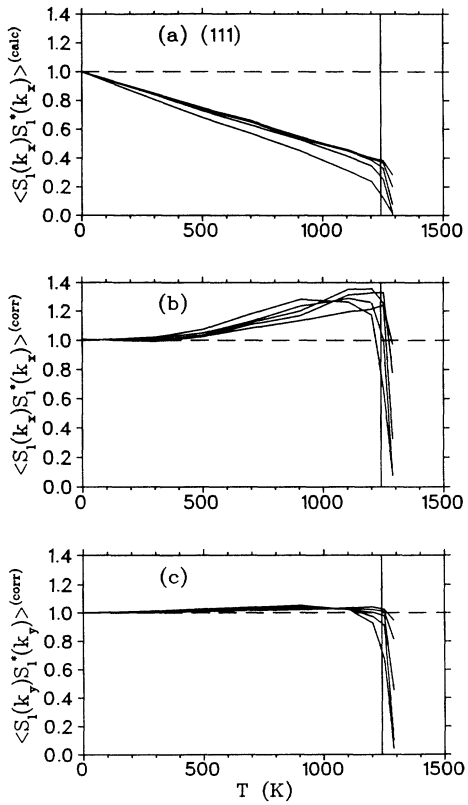

FIG. 7. The order parameter $\langle |S_l(\mathbf{k})|^2 \rangle$ as a function of temperature for the first five crystal layers of (111). (a) Calculated and (b) corrected values for $\mathbf{k}=(4\sqrt{2}\pi/a)(1,0)$; (c) corrected values for $\mathbf{k}=(4\sqrt{2}\pi/\sqrt{3}a)(0,1)$.

The vertical lines in Figs. 5–7 indicate the estimated thermodynamical melting point in our model potential. Below T_m, the disorder is most pronounced on (110), much weaker on (100), and (111) is seen to be very well ordered up to T_m. The corrected order parameter for the (110) surface layer decreases a little faster in the direction of the nearest-neighbor chains (y direction) [Fig. 5(c)] than perpendicular to the chains [Fig. 5(b)]. A weak anisotropy in the disordering of the (110) metal surface has also been seen in experiments.[9]

We have to comment on the peculiar behavior of the corrected order parameter in the x direction on (111) [Fig. 7(b)], since it includes an important limit of validity to our analysis of the order parameter. The rise of the order parameter between 400 and 1100 K can be understood by noticing first that the magnitude of the reciprocal-lattice vector in that direction is the greatest among the vectors studied. Writing $\mathbf{r}_j=\mathbf{r}_{j0}+\mathbf{u}_j$, and by expanding Eq. (4) as a power series around the lattice site $\mathbf{r}_{j0}$,

$$|S_l(\mathbf{k})|^2=1-k^2\langle u^2\rangle+k^4\langle u^4\rangle-\cdots , \tag{6}$$

we see that the fourth-order term in our corrected order parameter would then be $e^{-(1/4)k^4\langle u^4\rangle}$. Now, when $|\mathbf{k}|$ becomes large enough, this fourth-order correction should be taken into account. By carefully inspecting the calculated order parameters of (111) in the x direction [Fig. 7(a)], we can see that it is the only case where the uncorrected order parameter has an *upward* curvature below 1000 K. Since the second term in the right-hand side of Eq. (6) produces a downward curvature in the calculated order parameter, Fig. 7(a) indeed implies that the third term $k^4\langle u^4\rangle$ in Eq. (6) becomes important in the x direction on (111). This shows the range of reciprocal vectors within which our analysis, based on the correction in the form expressed in Eq. (5), is valid.

B. Layer occupation and energetics

The occupation of surface layers at different temperatures beyond 600 K is shown in Fig. 8 for all studied faces. On (110), the formation of the adatom layer begins around 700 K and the related vacancies are found in the first crystal layer at temperatures of 700–1000 K. Beyond 1000 K, atoms from deeper crystal layers also begin to diffuse to the surface, enhancing the formation of the adatom layer. Finally, around T_m the atomic density of the surface layer begins to *increase* due to the fact that the atoms in the surface layer can improve their coordination when the surface liquid becomes thick enough. On (100) and (111), the onset of the vacancy-adatom formation takes place at higher temperatures (900 and 1100 K, respectively), and practically all adatoms come from the first crystal layer. The behavior of (110) agrees with

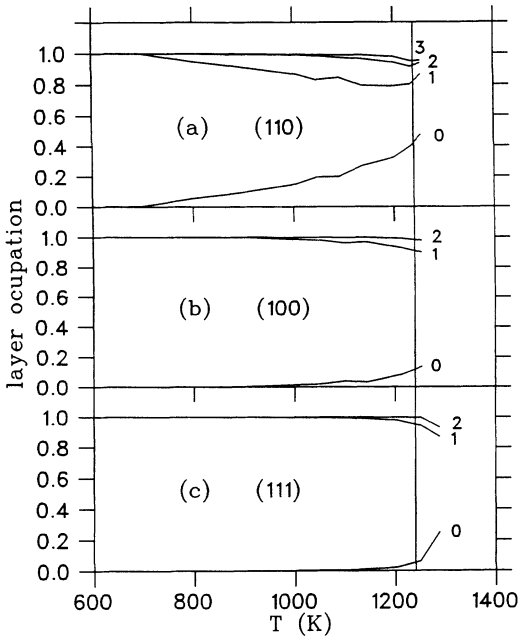

FIG. 8. The layer occupation (in monolayers) as a function of temperature for the adatom layer on and the first few crystal layers of (a) (110), (b) (100), and (c) (111).

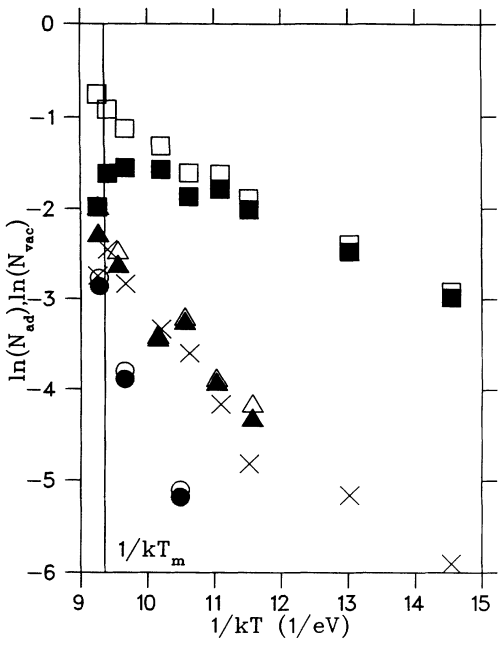

FIG. 9. The natural logarithm of the vacancy concentration N_{vac} in the first crystal layer (filled symbols) and adatom concentration N_{ad} (open symbols) as a function of $1/kT$ on (110), (100), and (111) (denoted by squares, triangles, and circles, respectively). The crosses show the logarithm of the vacancy concentration in the second crystal layer of (110). The vertical line shows $1/kT_m$.

gradual thickening of the defective surface area, which is a precursor phase of premelting also in simulations of Al(110) (Ref. 29) and Ni(110),[30] and more recently of Cu(110) using the EAM potential.[32] Experimentally, the transition observed in this temperature region is often interpreted as surface roughening. We want to emphasize that the MD investigation of the "true" roughening transition, characterized by the logarithmic divergence of the height-height correlation function,[14,15] is seriously affected by the finite-size limitations in simulation time and sample size. Very recently, however, Monte Carlo (MC) calculations employing practically the same potential for Cu as what is used in this work have shown that, when depositing copper atoms on Cu(110), the growth mechanism of the surface has a transition from a layer-by-layer growth to a continuous growth around 900 K.[69] This is a sign of a true roughening transition, and at present we are planning extensive simulations combining both MC and MD methods to investigate the nature and the dynamics of this transition.

In Fig. 9 we have drawn the concentrations of vacancies in the first crystal layer and of adatoms on each face in the Arrhenius form. The energies of the vacancy-adatom formation in the surface layer are estimated to be 0.39, 0.86, and 1.92 eV for (110), (100), and (111), respectively. By using the nearest-neighbor EMT, we have estimated the (unrelaxed) formation energy of the vacancy-adatom pair at $T=0$ to be 0.55 eV for (110) and 1.8 eV for (111). The low energy for the defect formation on (110) correlates with the tendency of that face to disorder far below T_m. The formation energy obtained by the Arrhenius plot for (110) is probably due to many different defect mechanisms. The recent EAM simulation for Ni(110) (Ref. 30) showed that it is energetically more favorable for that face to form a pair of a *divacancy* and two adatoms than to form two independent vacancy-adatom pairs. We have not studied in detail the vacancy-adatom formation mechanism, but snapshots (Sec. VI E) indeed imply the existence of divacancies.

Figure 10 shows the energetics of surface layers at elevated temperatures. When comparing the different faces, the most interesting features are displayed by the (110) surface. During premelting, there seems to be no discontinuity and subsequent latent heat in the first three crystal layers, latent heating being visible for $l>4$ (not shown in Fig. 10). Theoretically, it has been shown that a first-order phase transition in a semi-infinite system can involve critical surface effects that make the transition continuous on the surface.[17] Our results also support interpretation of the melting mechanism of (110) having a tendency toward facet formation in the solid-quasiliquid interface, rather than being layerwise. The melting mechanisms in different directions are discussed in more detail in Sec. VI F.

The statistics of adatoms are quite poor, resulting in large fluctuations in the adatom energies. However, on (110) and (100) the energy of the adatom layer is seen to systematically decrease with increasing occupation at high temperatures. This results from clustering effects, which are visible in snapshots (Sec. VI E). Those adatoms that appear in Fig. 10 below the onset of the actual adatom layer formation [at 700 and 1000 K for the (110) and (100) faces, respectively] are, in fact, atoms which belong to the first crystal layer but are vibrating with so

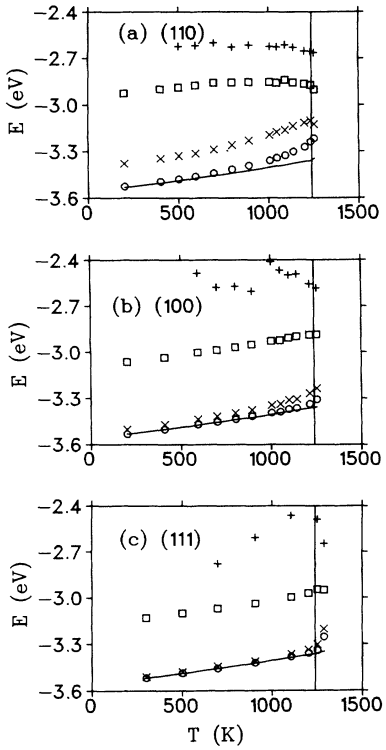

FIG. 10. The potential energy per atom as a function of temperature for the surface layers of (a) (110), (b) (100), and (c) (111). Pluses, $l=0$ (adatoms); squares, $l=1$; crosses, $l=2$; circles, $l=3$; and solid line, $l=10$ (bulk).

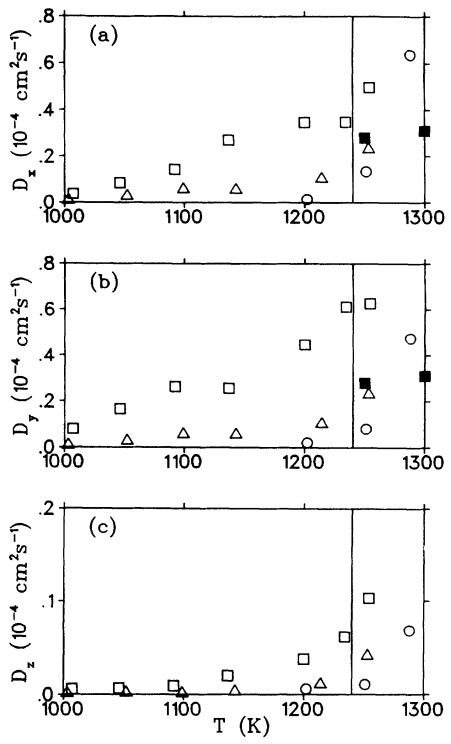

FIG. 11. The diffusion constant as a function of temperature for the first crystal layer of (110), (100), and (111) calculated (a) in the x direction, (b) in the y direction, and (c) in the z direction. The open squares are for (110), the triangles are for (100), and the circles are for (111). The filled squares in (a) and (b) show the calculated D_x in the bulk liquid at 1250 and 1300 K.

large an amplitude that they are occasionally counted as adatoms, or they belong to short-lived vacancy-adatom pairs.

C. Diffusion

In order to compare the dynamical properties of (110), (100), and (111) at high temperatures, we have studied the diffusion constant D of surface layers, which is known to be related to the long-time behavior of the mean-square deviation,

$$u^2(t)=2d\,Dt, \quad \text{when } t\rightarrow\infty\ , \tag{7}$$

where d is the dimension of the space for which u^2 is determined. The diffusion constants calculated separately in the x, y, and z directions are plotted in Fig. 11 for the first crystal layer of each face. In calculating D_x and D_y, we have concentrated on the in-plane diffusion, which means that if an atom is found to move away from layer l, its contribution to the MSD of l is no longer included.

We have determined the one-dimensional diffusion constant to be 0.3×10^{-4} cm^2 s^{-1} from the MD calculations for bulk liquid copper at 1250 K, in reasonable agreement with the experimental value of 0.4×10^{-4} cm^2 s^{-1} near the melting point.[70] It can be seen from Fig. 11 that, well below the bulk melting point, the in-plane diffusion on (110) is comparable to that in the bulk liquid just above T_m and becomes even faster just below T_m. This is consistent with the concept of premelting, which involves the growth of a highly mobile liquidlike film on the surface.[71] Diffusion is slightly enhanced in the direction of the nearest-neighbor rows (y direction) on (110), which results from the crystallographic anisotropy of that face. It is also natural that diffusion in the direction perpendicular to the surface cannot be as large as that parallel to the surface because the quasiliquid thickness in our calculations is at most a few atomic layers. The diffusion constant in the first crystal layer of (100) does not reach the value typical in the bulk liquid below our estimated T_m, and is practically zero in the first (111) crystal layer showing the much weaker disordering of (100) and the absence of premelting of (111).

D. Pair correlation functions

In addition to structure factors, we have calculated 2D pair correlation functions at elevated temperatures in order to study the crystalline order of the surface layers of each face. The 2D pair correlation function $g_l(r)$ is defined as

$$g_l(r)=\left\langle \frac{A}{N_l}\,\frac{n(r,r+\Delta r)}{2\pi r\Delta r}\right\rangle , \tag{8}$$

where A is the layer area, N_l the instantaneous number of atoms in layer l, $n(r,r+\Delta r)$ the number of neighbors

within the distance $(r, r+\Delta r)$, and $\langle\ \rangle$ denotes the average over atoms and time. $g(r)$ expresses the probability of finding a pair of atoms separated by a distance in the interval $(r, r+\Delta r)$, both atoms belonging to the same crystal layer l.

$g_l(r)$ for the first crystal layer of (110) is plotted at elevated temperatures in Fig. 12. It is clear that the crystallographic order of the surface disappears gradually when T_m is approached. We can safely conclude that the surface is in a liquid state at 1254 K, where $g_l(r)$ shows only short-range order typical for liquids. From the pair correlation function we conclude that the premelting of (110) takes place at $T \geq 1200$ K, where the long-range oscillation (around $r = 20a_0$) in $g_l(r)$ disappears. Figure 13 shows $g_l(r)$ for ten layers, numbered from the surface, of (110) at 1200 and 1254 K. The quasiliquid thickness rises up to approximately five atomic layers in this temperature region. We interpret 1254 K to be very close to the solid-liquid coexistence point, since a small amount of heating above this temperature clearly results in melting of the bulk crystal. This result is in good agreement with the estimate of 1240±25 K which we find by extrapolating the velocity of the melting front to zero.

Figures 14 and 15 show $g_l(r)$ at elevated temperatures for the first crystal layers of (100) and (111), respectively. Both faces show crystalline order up to ≈1250 K. The (111) face is seen to melt somewhere between 1251 and 1288 K, the surface layer being clearly liquidlike at 1288 K.

In conclusion from the analysis based on the pair correlation function and diffusion coefficient, melting of the (110) face nucleates around 1200 K, i.e., about 40–50 K below the estimated thermodynamical melting point. The maximum thickness of the quasiliquid we have observed is about five atomic layers. In contrast with this, both the (100) and (111) faces preserve their crystalline order practically up to T_m [and (111) maybe to even higher temperatures]. These observations correlate very well with the experiments on the surface melting of metals,[4–8,11] with the recent intriguing result of superheating of Pb crystallites which have only (111) facets,[72] and with a MD study of Au(111).[31] The nonmelting behavior of Cu(111) is in striking disagreement with the Lennard-Jones (111) surface, which shows clear premelting effects below the triple point.[25]

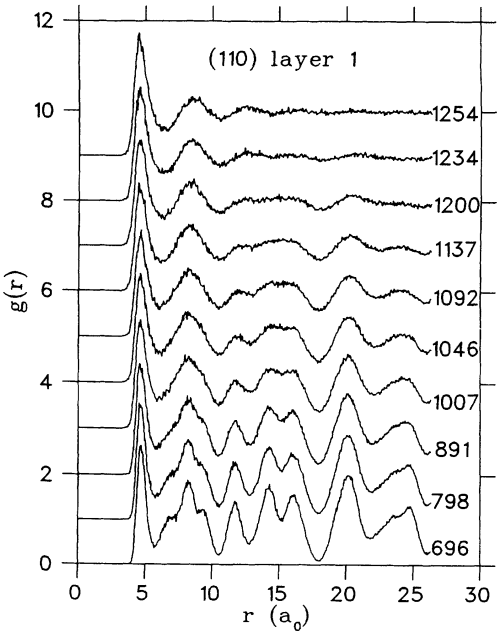

FIG. 12. The two-dimensional pair correlation function $g(r)$ for the first crystal layer of (110) at elevated temperatures.

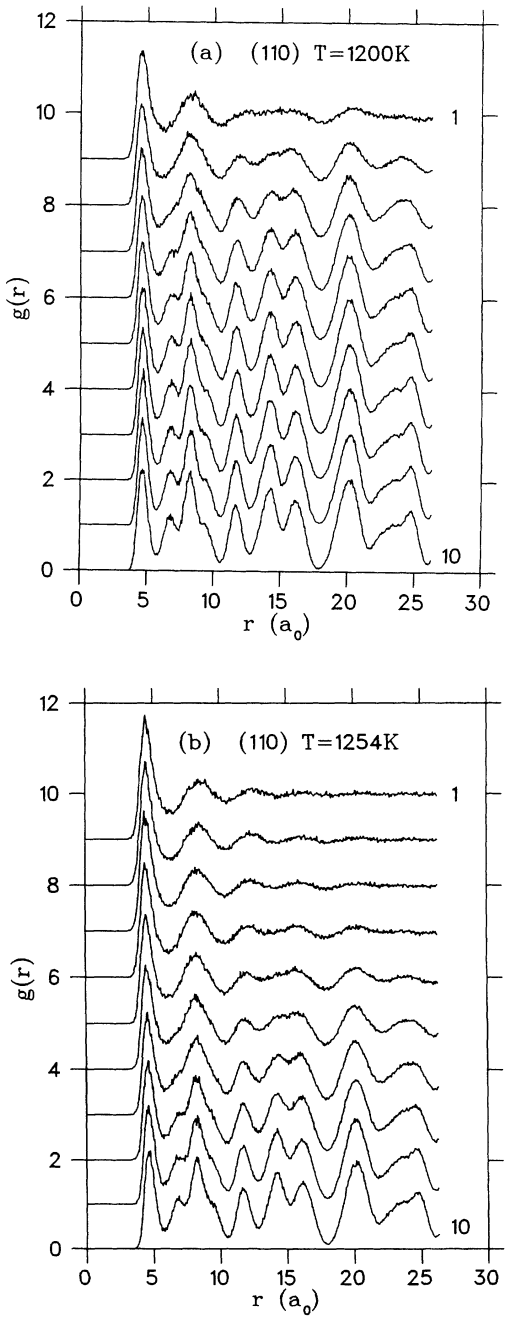

FIG. 13. The two-dimensional pair correlation function $g(r)$ for the first ten crystal layers of (110) at $T = 1200$ K and (b) $T = 1254$ K.

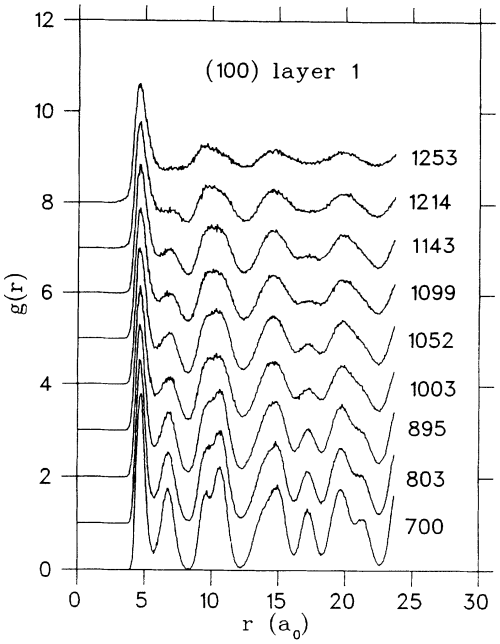

FIG. 14. Same as Fig. 12, but for the (100) face.

E. Snapshots and trajectory plots

In order to complete the quantitative analysis of disordering and premelting that has been described in Secs. VI A–VI D we shall next visualize our calculations by means of snapshots and trajectory plots. Figure 16 shows a series of snapshots of equilibrium configurations of (110). Adatoms begin to appear on the surface beyond 700 K (a) leading eventually to the planar disorder at and above 1200 K (d) and (e). The snapshots at (b) 1007 K and (c) 1092 K show the adatom clustering effect and also support the assumption of the formation of divacancies in the first crystal layer (see Sec. VI B). The premelted surface at 1200 K begins to show signs of a *hexagonal* order, which is typical for a liquid metal surface.[73]

A dynamical view of the disordering of the (110) face is shown in Fig. 17, which shows the trajectories of atoms over a short time span, projected into a plane perpendicular to the surface. The trajectory plots support the vacancy-adatom mechanism of disordering, where the thickness of the defective surface region is gradually increased with increasing temperature. Beyond 1200 K the crystal geometry cannot be observed in the trajectories of the surface atoms, and the quasiliquid region begins to grow.

Figure 18 provides visual support for the main conclusion of our work: surface stability is related to the packing density. Practically at T_m, the (110) face clearly has a liquidlike surface region, on the (100) face weak disorder is observable only in the first crystal layer, and the (111) face is clearly in a crystalline state with only a few vacancies in the first layer and related adatoms diffusing above the surface.

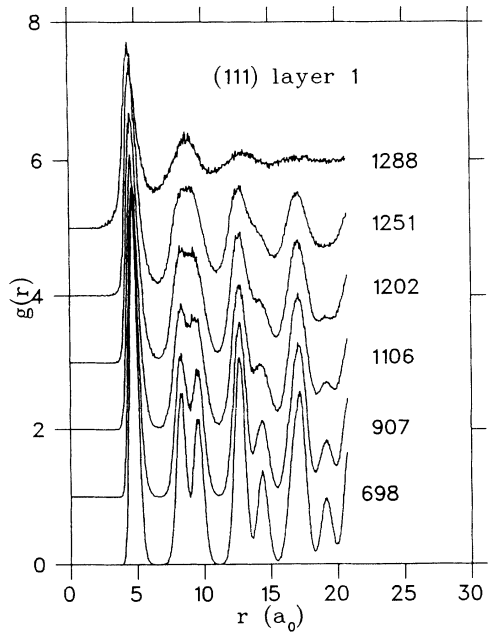

FIG. 15. Same as Fig. 12, but for the (111) face.

F. Solid-quasiliquid interface

An interesting observation can be made by comparing Figs. 18(a) and 19, which view the (110) solid-quasiliquid interface from the ⟨110⟩ and ⟨100⟩ directions, respectively. It is clear that the interface is quite sharp when viewed from the ⟨100⟩ direction, whereas it is broad and weakly faceted in the ⟨110⟩ direction. The broadening of the interface is also seen by inspecting the atomic-density profile across the sample shown in Fig. 20. On the other hand, the (111) solid-quasiliquid interface, shown in Fig. 21, is quite sharp. These observations can be understood as follows. Since the atoms moving in the liquid near the interface feel the underlying periodic potential, the liquid has a tendency to exhibit residual crystal order. The free energy associated with the (111) interface is expected to be low, since it is energetically easy to form close-packed *liquid layers,*[56] but near the (110) interface close packing is only possible in the direction parallel to the underlying nearest-neighbor rows. This leads to an anisotropic structure of liquid near the interface. Another possibility for decreasing the interfacial energy is to form atomic-scale (111) facets. This phenomenon grows stronger as the difference between the free energies of the (110) and (111) solid-liquid interfaces increases. This mechanism has been found for Si(100) in MD calculations which employ the Stillinger-Weber potential.[26–28] Figure 18 indeed gives implications of faceting, although it is not as strong as on Si(100). The melting mechanism of the (100) and (111) faces seems to be more like a layer-by-layer mechanism, as implied by the structure of the (111) solid-quasiliquid interface (Fig. 21). Qualitatively, the melting mechanism of this surface is therefore similar to that of a (111) Lennard-Jones surface,[25] despite the lack of premelting.

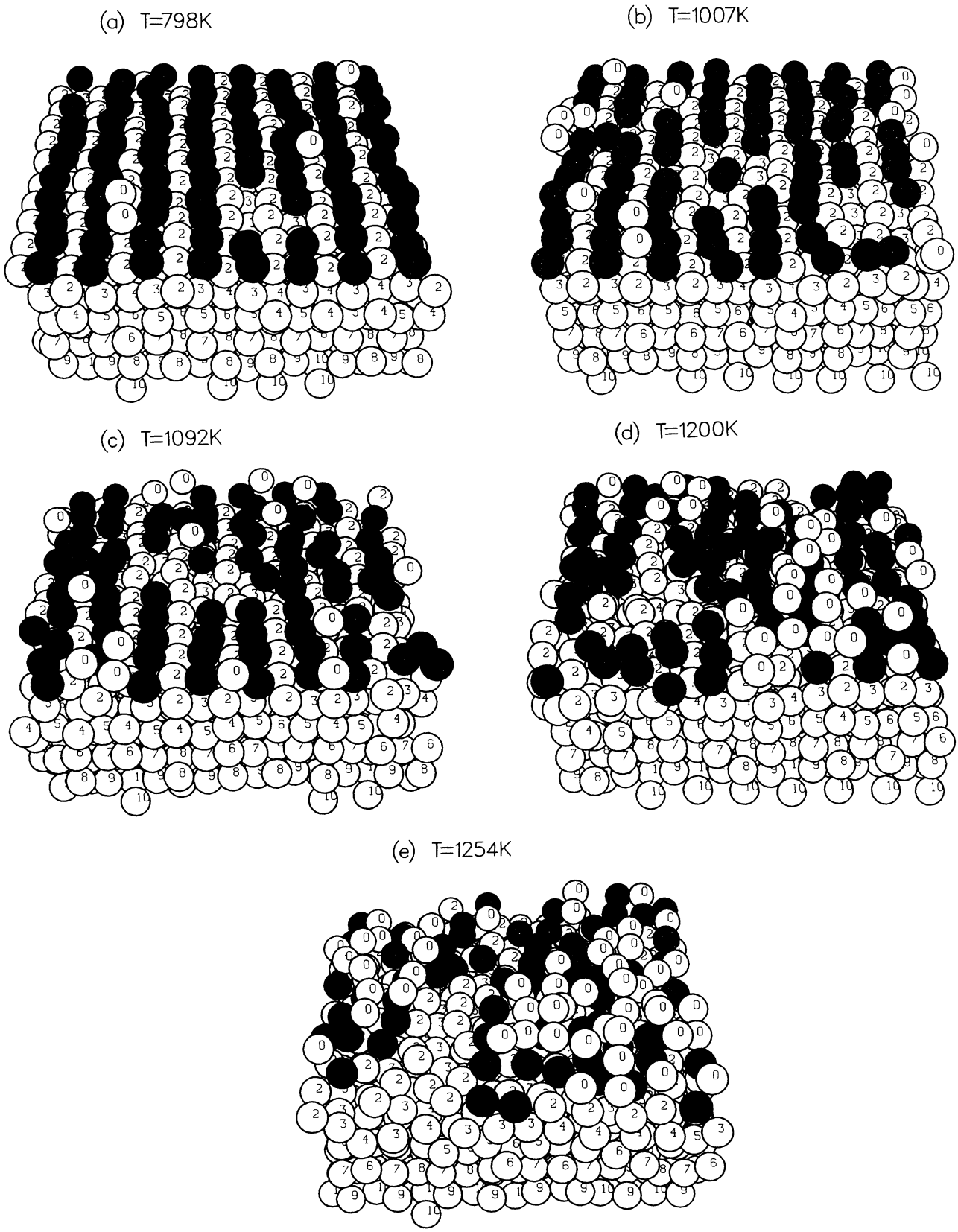

FIG. 16. Snapshots of configurations of (110) at (a) 798 K, (b) 1007 K, (c) 1092 K, (d) 1200 K, and (e) 1254 K. The numbers denote the crystal layers. The black atoms belong to the first crystal layer.

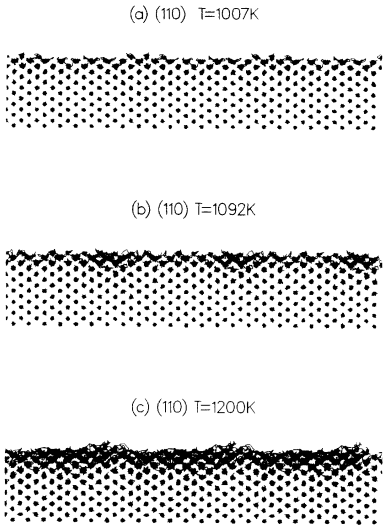

FIG. 17. Atomic trajectories (viewed from the ⟨110⟩ direction) on (110) projected onto a plane perpendicular to the free surface at (a) 1007 K, (b) 1092 K, and (c) 1200 K. The time span for the motion is about 4 ps. Three computational cells are shown in the horizontal direction, whereas half of the dynamical layers are shown in the vertical direction.

VII. CONCLUSIONS

In this work we have presented a coherent approach to the surface disordering and premelting phenomena on low-index faces of copper using the MD method with a realistic many-atom potential. The main results can be concluded as follows. The order in the surface stability follows the order in the packing density. The (110) face disorders first by anharmonic effects (up to 700 K), then by vacancy-adatom formation, and finally by premelting at around 1200 K. The estimated thermodynamical melting point T_m is 1240±25 K in our model. This result is in quantitative agreement with a recent independent EAM study of Cu(110),[32] where premelting was observed to nucleate around 1200 K, the estimated T_m being 1284±10 K. The (100) face disorders only weakly just below T_m. The (111) face is in a crystalline state practically up to T_m and shows weak superheating effects. The observed order in the surface stability is the same as that seen in experiments of fcc metals. The superheating property of the (111) face correlates well with the recent observations of superheated metal crystallites that have close-packed surfaces,[72] and also with the proposed nonmelting or blocked-melting behavior of Au(111) in the MD calculations.[31] The (110) solid-quasiliquid interface is broadened and anisotropic and shows a tendency to form atomic-scale (111) facets in equilibrium. Faceting of a loose-packed face is proposed to be the dominant atomic-scale surface-initiated melting mechanism in metals compared to the more layerwise melting of the (100) and (111) faces.

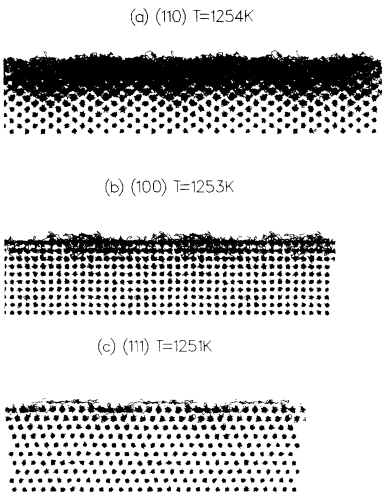

FIG. 18. Atomic trajectories near the bulk melting point T_m on (a) (110), (b) (100), and (c) (111). The sample is viewed from the ⟨110⟩, ⟨100⟩, and ⟨110⟩ directions in (a), (b), and (c), respectively. Note the weak faceting of the (110) solid-quasiliquid interface and the stability of the (111) face.

FIG. 19. The structure of the (110) solid-quasiliquid interface near T_m viewed from the ⟨100⟩ direction. Compare with Fig. 18(a).

ACKNOWLEDGMENTS

Fruitful discussions with J. W. M. Frenken, U. Landman, J. Merikoski, J. Timonen, and S. Valkealahti are gratefully acknowledged. This work has been partly (H.H.) supported by the Emil Aaltonen Foundation. The

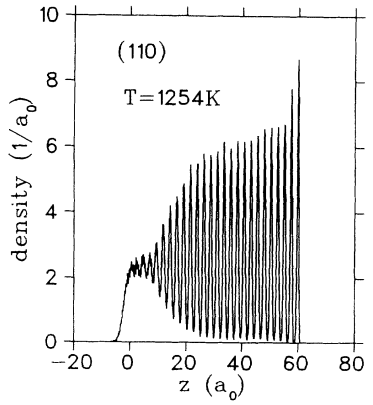

FIG. 20. The number density of atoms in the sample with one free (110) surface near T_m. The surface layer is located at $z=0$ at $T=0$. The two sharp peaks on the right-hand side of the sample are due to the adjacent static crystal layers.

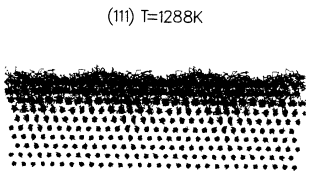

FIG. 21. The structure of the solid-quasiliquid interface on (111) at 1288 K.

main part of the computations has been made using the Cray X-MP at the Centre for Scientific Computing (CSC) in Espoo, Finland.

APPENDIX A: THE NOSÉ-HOOVER THERMOSTAT AND THE VELOCITY-VERLET ALGORITHM

In the Nosé-Hoover thermostat,[38] the temperature of the system is controlled by a feedback in equations of motion through an auxiliary degree of freedom ξ,

$$\mathbf{a}_i=\frac{\mathbf{F}_i}{m_i}-\xi\mathbf{v}_i\ ,\qquad \dot{\xi}=\frac{T-T_{\rm ref}}{\tau^2 T_{\rm ref}}\ , \tag{A1}$$

where m_i, $\mathbf{v}_i$, and $\mathbf{a}_i$ are the mass, velocity, and acceleration of atom i, respectively, $\mathbf{F}_i$ is the total interatomic force on atom i, τ is an arbitrary thermostat relaxation time, T is an instantaneous (kinetic) temperature, and $T_{\rm ref}$ is the desired long-time average for the temperature.

The velocity-Verlet algorithm is a version of Verlet-type algorithms where atomic positions and velocities are handled simultaneously.[39] Denoting by h the time step, the positions and velocities are advanced from time t to $t+h$ such that

$$\mathbf{r}(t+h)=\mathbf{r}(t)+h\mathbf{v}(t)+\tfrac{1}{2}h^2\mathbf{a}(t)\ ,\qquad \mathbf{v}(t+h)=\mathbf{v}(t)+\tfrac{1}{2}h[\mathbf{a}(t)+\mathbf{a}(t+h)]\ . \tag{A2}$$

In order to solve the equations of motion (A1) with (A2) we have assumed a simple centered-difference estimate for $\dot{\xi}$,

$$\dot{\xi}(t)\approx\frac{\xi(t+h)-\xi(t-h)}{2h}\ . \tag{A3}$$

Assuming that atomic positions, velocities, and accelerations are known at some time t, the MD cycle then consists of the following steps.

(i) Advance the positions to $\mathbf{r}(t+h)$ [first part of (A2)], calculate the value for ξ

$$\xi(t+h)=\xi(t-h)+2h[T(t)-T_{\rm ref}]/(\tau^2 T_{\rm ref})\ , \tag{A4}$$

and take a half step for velocities

$$\mathbf{v}(t+h/2)=\mathbf{v}(t)+h\mathbf{a}(t)/2\ . \tag{A5}$$

(ii) Calculate forces $\mathbf{F}(\mathbf{r}(t+h))$.

(iii) Advance velocities to $t+h$ such that

$$\mathbf{v}(t+h)=\left[\mathbf{v}(t+\tfrac{1}{2}h)+\frac{1}{2}\frac{\mathbf{F}(t+h)}{m}\right]\Big/[1+\tfrac{1}{2}h\xi(t+h)]\ , \tag{A6}$$

and calculate accelerations $\mathbf{a}(t+h)$ from Eq. (A1).

The time step used in most of our calculations has been 14 fs, which is fairly large, being roughly a tenth of the fastest vibration period in the copper lattice. This large time step still produces a rms fluctuation of total energy which is less than 0.2 meV/atom for tens of picoseconds in microcanonical simulations. The good energy conservation implies that the velocity-Verlet algorithm is one of the most stable algorithms for MD.

APPENDIX B: TECHNICAL DETAILS OF EMT

This Appendix discusses the modifications made in this work to the nearest-neighbor EMT formalism described in Ref. 35. To summarize the original scheme, the calculation of the total energy $E_{\rm tot}$ of N arbitrarily arranged metal atoms is performed in the following way:

$$\begin{aligned}
&E_{\rm tot}=\sum_{i=1}^{N}E_C(\bar{n}_i)+E_{\rm AS}\ ,\\
&E_C=E_0+E_2\left[\frac{\bar{n}}{n_0}-1\right]^2+E_3\left[\frac{\bar{n}}{n_0}-1\right]^3\ ,\\
&\bar{n}_i=n_0 e^{-\eta(s_i-s_0)}\ ,\\
&s_i=-\frac{1}{\beta\eta_2}\ln\left[\frac{1}{12}\sum_{j\neq i}^{\rm NN}\rho(r_{ij})\right]\ ,\\
&\rho(r)=e^{-\eta_2 r}\ ,\\
&E_{\rm AS}=\sum_{i=1}^{N}\alpha\left[\bar{n}_i-\frac{n_0}{12}\sum_{j\neq i}^{\rm NN}\rho^{\rm fcc}(r_{ij})\right]\ ,\\
&\rho^{\rm fcc}(r)=e^{-\eta(r/\beta-s_0)}\ .
\end{aligned} \tag{B1}$$

The main part of the cohesion comes from the E_C term, which gives the energy when an atom is embedded in the homogeneous electron gas having a density equal to the local electronic density $\bar{n}_i$ averaged over a sphere of radius s_i. $E_{\rm AS}$ is the so-called atomic-sphere correction. which gives the energy of distortions from the ideal fcc symmetry. Physically, it represents the electrostatic energy when neighboring (neutral) Wigner-Seitz spheres are forced to overlap. It is assumed that the electrostatic energy associated with overlaps and holes of neighboring Wigner-Seitz spheres cancel in an ideal fcc lattice, and $E_{\rm AS}$ is therefore zero. NN in the sums for ρ and $\rho^{\rm fcc}$ means that only the density tails from the nearest neighbors are considered in the calculation of $\bar{n}_i$. A detailed discussion of EMT is given in Refs. 35 and 53. The parameters used for copper are given in Ref. 37.

In this work, we have made three modifications to the scheme outlined above. First, we have shifted the zero-density limit in the total energy to zero by adding a term $(E_3-E_0-E_2)e^{-30\bar{n}/n_0}$ to the third-order expansion of

E_C in Eq. (B1). This correction is damped very quickly when the density is increased and it has no effect on the total energy in densities normally found for surface atoms. We wanted to correct the zero-density limit, since if a surface atom would occasionally gain enough energy to escape from the surface to vacuum (a rare, but possible event for the uncorrected potential), the EMT formalism would technically fail due to the logarithm of zero in the expression for s in (B1). It is also physically reasonable that copper atoms do not move into vacuum in the time and spatial scale of a MD simulation.

The other modifications have been made in order to extend the range of the potential self-consistently beyond the nearest neighbors and to introduce a shifted-force cutoff for the interactions. The self-consistency requirement means that the calculated electron densities must be normalized to correspond to the densities of the nearest-neighbor formalism in such a way that the total energy vs lattice-parameter curve for the ideal fcc lattice remains unchanged. We have set the cutoff radius r_c in the middle of the distance between the third and fourth neighbors in the zero-temperature copper lattice, and modified the density tails ρ and $\rho^{\rm fcc}$ to have the potential and force to go smoothly to zero at the cutoff:

$$\rho(r)\rightarrow\rho(r)-\rho(r_c)-(r-r_c)\left.\frac{d\rho}{dr}\right|_{r=r_c},$$
$$\rho^{\rm fcc}(r)\rightarrow\rho^{\rm fcc}(r)-\rho^{\rm fcc}(r_c)-(r-r_c)\left.\frac{d\rho^{\rm fcc}}{dr}\right|_{r=r_c}. \tag{B2}$$

When the second and the third neighbors are included, the atomic-sphere radius s_i is written for an ideal fcc lattice as

$$s_i=-\frac{1}{\beta\eta_2}\ln\left\{\frac{1}{12\gamma_1}\{12[e^{-\eta_2\beta s_i}-e^{-\eta_2 r_c}+(\beta s_i-r_c)\eta_2 e^{-\eta_2 r_c}]+6[e^{-\sqrt{2}\eta_2\beta s_i}-e^{-\eta_2 r_c}+(\sqrt{2}\beta s_i-r_c)\eta_2 e^{-\eta_2 r_c}]\right.$$
$$\left.+24[e^{-\sqrt{3}\eta_2\beta s_i}-e^{-\eta_2 r_c}+(\sqrt{3}\beta s_i-r_c)\eta_2 e^{-\eta_2 r_c}]\}\right\}, \tag{B3}$$

where γ_1 is a normalization factor. Equaling this with the nearest-neighbor expression for s_i in (B1), γ_1 turns out to be

$$\gamma_1(s_i)=1+\tfrac{1}{2}e^{(1-\sqrt{2})\eta_2\beta s_i}+2e^{(1-\sqrt{3})\eta_2\beta s_i}+e^{\eta_2(\beta s_i-r_c)}[\eta_2\beta s_i(1+\tfrac{1}{2}\sqrt{2}+2\sqrt{3})-3\tfrac{1}{2}(1+\eta_2 r_c)]. \tag{B4}$$

The nearest-neighbor expression for s_i in Eq. (B1) is thereby generalized to

$$s_i=-\frac{1}{\beta\eta_2}\ln\left[\frac{1}{12\gamma_1(s_i)}\sum_{j\neq i}\left[\rho(r_{ij})-\rho(r_c)-(r_{ij}-r_c)\times\left.\frac{d\rho}{dr}\right|_{r=r_c}\right]\right]. \tag{B5}$$

This implicit equation for s_i is solved iteratively (usually 5–10 iterations is sufficient to solve s_i with six significant figures), and the calculation of $\bar{n}$ and E_C then goes as described in (B1). The expression for $E_{\rm AS}$ is modified such that

$$E_{\rm AS}=\sum_{i=1}^{N}\alpha\left[\bar{n}_i-\frac{n_0}{12\gamma_2(s_i)}\times\sum_{j\neq i}\left[\rho^{\rm fcc}(r_{ij})-\rho^{\rm fcc}(r_c)-(r_{ij}-r_c)\left.\frac{d\rho}{dr}\right|_{r=r_c}\right]\right], \tag{B6}$$
$$\gamma_2(s_i)=1+\tfrac{1}{2}e^{(1-\sqrt{2})\eta s_i}+2e^{(1-\sqrt{3})\eta s_i}+e^{\eta(s_i-r_c)}[\eta s_i(1+\tfrac{1}{2}\sqrt{2}+2\sqrt{3})-3\tfrac{1}{2}(1+\eta r_c)].$$

In our previous bulk calculations with the extended interactions, the implicit equation for s_i was solved by calculating at each time step the normalization factors $\gamma_1(s)$, $\gamma_2(s)$ from the averaged atomic-sphere radius $\bar{s}$.[37] The present method is a generalization of our previous method to systems that have a crystal surface, where the use of an averaged atomic-sphere radius would be unreasonable because the value of $\bar{s}$ depends on the surface-to-volume ratio. The iterative solution of s_i's does not make the calculation much slower, especially in vector machines, where one iteration loop over atoms can be vectorized. The calculation of the total energy and forces in one MD time step requires typically 0.5–1.0 CPU seconds for $N\approx 2000$ atoms on one processor of Cray X-MP. The present scheme is then applicable to much

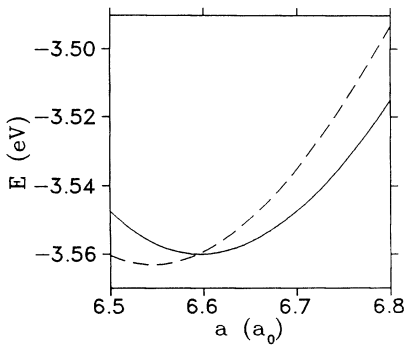

FIG. 22. The potential energy of an ideal $T=0$ copper lattice as a function of the lattice parameter. The solid line is for the nearest-neighbor EMT, the dashed line is for the case where interactions are extended to the third-nearest neighbors, but the densities are calculated in a non-self-consistent way.

larger systems than those considered in this work.

In Refs. 29, 33, and 35 the normalization factors γ_1 and γ_2 are taken as constants, the values of which depend only on the cutoff radius, not on s_i's. This has the effect that the total energy vs lattice-parameter curve calculated with the extended interactions deviates from the result from the nearest-neighbor formalism. For example, by including the third neighbors in copper, this deviation is at most 20 meV/atom for reasonable lattice parameters, as seen in Fig. 22. The minimum in the total energy is shifted to larger densities, which causes the zero-temperature lattice parameter to decrease by about 1%. The difference comes from the E_{AS} term, which should be zero for the ideal fcc lattice regardless of the range of the interactions. We expect that the essential physics resulting from the use of EMT is not qualitatively affected by minor variations in the way by which the interactions are extended beyond the nearest neighbors in Refs. 29, 33, 35, and in our work, but phenomena such as surface disordering and premelting are likely to be shifted to somewhat higher temperatures if a non-self-consistent method is used, due to the increase in density and subsequent extra cohesion and stability in the crystal.

[1]For reviews, see J. F. van der Veen, B. Pluis, and A. W. Denier van der Gon, in *Chemistry and Physics of Solid Surfaces VII,* edited by R. Vanselow and R. F Howe (Springer, Berlin, 1988); J. G. Dash, Contemp. Phys. **30**, 89 (1989).

[2]M. Faraday, Proc. R. Soc. London, Ser A **10**, 440 (1860).

[3]G. Tammann, Z. Phys. Chem. **68**, 205 (1910); Z. Phys. **11**, 609 (1910).

[4]K. D. Stock and E. Menzel, Surf. Sci. **61**, 272 (1976).

[5]K. D. Stock and E. Menzel, J. Cryst. Growth **43**, 135 (1978).

[6]K. D. Stock, Surf. Sci. **91**, 655 (1980).

[7]J. W. M. Frenken and J. F. van der Veen, Phys. Rev. Lett. **54**, 134 (1985).

[8]J. W. M. Frenken, P. M. J. Marée, and J. F. van der Veen, Phys. Rev. B **34**, 7506 (1986).

[9]K. C. Prince, U. Breuer, and H. P. Bonzel, Phys. Rev. Lett. **60**, 1146 (1988).

[10]P. von Blanckenhagen, W. Schommers, and V. Voegele, J. Vac. Sci. Technol. A **5**, 649 (1987).

[11]A. W. Denier van der Gon, R. J. Smith, J. M. Gay, D. J. O'Connor, and J. F. Van der Veen, Surf. Sci. **227**, 143 (1990).

[12]H. Dosch, T. Höfer, J. Peisl, and R. L. Johnson, Europhys. Lett. **15**, 527 (1991).

[13]Da-Ming Zhu and J. G. Dash, Phys. Rev. Lett. **57**, 2959 (1986); *ibid.* **60**, 432 (1988); Phys. Rev. B **37**, 5586 (1988).

[14]W. Burton, N. Cabrera, and F. Frank, Philos. Trans. R. Soc. London, Ser. A **243**, 299 (1951).

[15]J. D. Weeks, in *Ordering in Strongly Fluctuating Condensed Matter Systems,* edited by T. Riste (Plenum, New York, 1980).

[16]B. Pluis, A. W. Denier van der Gon, J. W. M. Frenken, and J. F. van der Veen, Phys. Rev. Lett. **59**, 2678 (1987).

[17]R. Lipowsky and W. Speth, Phys. Rev. B **28**, 3983 (1983).

[18]B. Pluis, D. Frenkel, and J. F. van der Veen, Surf. Sci. **239**, 282 (1990).

[19]J. F. van der Veen, B. Pluis, and A. W. Denier ver der Gon, in *Kinetics of Ordering and Growth at Surfaces,* edited by M. G. Lagally (Plenum, New York, 1990).

[20]A. Trayanov and E. Tosatti, Phys. Rev. Lett. **59**, 2207 (1987).

[21]L. Pietronero and E. Tosatti, Solid State Commun. **32**, 255 (1979); C. S. Jayanthi, E. Tosatti, A. Fasolino, and L. Pietronero, Surf. Sci. **152/153**, 155 (1988).

[22]C. S. Jayanthi, E. Tosatti, and L. Pietronero, Phys. Rev. B **31**, 3456 (1985).

[23]J. Q. Broughton and L. V. Woodcock, J. Phys. C **11**, 2743 (1978); J. Q. Broughton and G. H. Gilmer, J. Chem. Phys. **79**, 5105 (1983).

[24]V. Rosato, G. Ciccotti, and V. Pontikis, Phys. Rev. B **33**, 1860 (1986).

[25]S. Valkealahti and R. M. Nieminen, Phys. Scr. **36**, 646 (1987).

[26]U. Landman, W. D. Luedtke, R. N. Barnett, C. L. Cleveland, M. W. Ribarsky, E. Arnold, S. Ramesh, H. Baumgart, A. Martinez, and B. Kahn, Phys. Rev. Lett. **56**, 155 (1986).

[27]F. F. Abraham and J. Q. Broughton, Phys. Rev. Lett. **56**, 734 (1986).

[28]J. Lampinen, R. M. Nieminen, and K. Kaski, Surf. Sci. **200**, 101 (1988).

[29]P. Stoltze, J. K. Nørskov, and U. Landman, Phys. Rev. Lett. **61**, 440 (1988); Surf. Sci. **220**, L693 (1989).

[30]E. T. Chen, R. N. Barnett, and U. Landman, Phys. Rev. B **41**, 439 (1990).

[31]P. Carnevali, F. Ercolessi, and E. Tosatti, Phys. Rev. B **36**, 6701 (1987); Surf. Sci. **189/190**, 645 (1987).

[32]R. N. Barnett and U. Landman, Phys. Rev. B **44**, 3226 (1991).

[33]A. W. Denier van der Gon, D. Frenkel, J. W. M. Frenken, R. J. Smith, and P. Stoltze, Surf. Sci. **256**, 385 (1991).

[34]*Many-Atom Interactions in Solids,* edited by R. M. Nieminen, M. J. Puska, and M. J. Manninen (Springer, Berlin, 1990).

[35]K. W. Jacobsen, J. K. Nørskov, and M. J. Puska, Phys. Rev. B **35**, 7423 (1987).

[36]M. S. Daw and M. I. Baskes, Phys. Rev. B **29**, 6443 (1984); S. M. Foiles, M. I. Baskes, and M. S. Daw, *ibid.* B **33**, 7983 (1986).

[37]H. Häkkinen and M. Manninen, J. Phys. Condens. Matter **1**, 9765 (1989).

[38]S. Nosé, Mol. Phys. **52**, 255 (1984); W. G. Hoover, Phys. Rev. A **31**, 1695 (1985).

[39]W. C. Swope, H. C. Andersen, P. H. Berens, and K. R. Wilson, J. Chem. Phys. **76**, 637 (1982).

[40]P. Stoltze, K. W. Jacobsen, and J. K. Nørskov, Phys. Rev. B **36**, 5035 (1987).

[41]H. Häkkinen and M. Manninen, Phys. Scr. **T33**, 210 (1990).

[42]H. Häkkinen, S. Mäkinen, and M. Manninen, Phys. Rev. B **41**, 12 441 (1990).

[43]K. W. Jacobsen and J. K. Nørskov, in *The Structure of Surfaces II,* edited by J. F. van der Veen and M. A. van Hove (Springer, Berlin, 1987); Phys. Rev. Lett. **60**, 2496 (1988).

[44]H. Häkkinen, J. Merikoski, and M. Manninen, J. Phys. Condens. Matter **3**, 2755 (1991).

[45]O. B. Christensen, P. Stoltze, K. W. Jacobsen, and J. K. Nørskov, Phys. Rev. B **41**, 12 413 (1990).

[46]O. B. Christensen, K. W. Jacobsen, J. K. Nørskov, and M. Manninen, Phys. Rev. Lett. **66**, 2219 (1991).

[47]M. J. Puska, R. M. Nieminen, and M. J. Manninen, Phys. Rev. B **24**, 3037 (1981).

[48]G. J. Ackland, G. Tichy, V. Vitek, and M. W. Finnis, Philos. Mag. A **56**, 735 (1987).

[49]R. P. Gupta, Phys. Rev. B **23**, 6265 (1981).
[50]D. L. Adams, H. B. Nielsen, J. N. Andersen, I. Stensgaard, R. Feidenhans'l, and J. E. Sørensen, Phys. Rev. Lett. **49**, 669 (1982).
[51]S. Å, Lindgren, L. Walldén, J. Rundgren, and P. Westrin, Phys. Rev. B **29**, 576 (1984).
[52]U. Landman, R. N. Hill, and M. Mostoller, Phys. Rev. B **21**, 448 (1980); R. N. Barnett, U. Landman, and C. L. Cleveland, *ibid.* **28**, 1685 (1983).
[53]K. W. Jacobsen, Comment. Condens. Matter Phys. **14**, 129 (1988); in *Many-Atom Interactions in Solids* (Ref. 34).
[54]W. R. Tyson and W. A. Miller, Surf. Sci. **62**, 267 (1977).
[55]J. F. Lutsko, D. Wolf, S. R. Phillpot, and S. Yip, Phys. Rev. B **40**, 2831 (1989); *ibid.* **40**, 2841 (1989).
[56]E. T. Chen, R. N. Barnett, and U. Landman, Phys. Rev. B **40**, 924 (1989).
[57]N. W. Ashcroft and N. D. Mermin, *Solid State Physics* (Holt, Rinehart and Winston, New York, 1981).
[58]M. Born and K. Huang, *Dynamical Theory of Crystal Lattices* (Oxford, London, 1962).
[59]S. G. J. Mochrie, Phys. Rev. Lett. **59**, 304 (1987).
[60]P. Zeppenfeld, K. Kern, R. David, and G. Comsa, Phys. Rev. Lett. **62**, 63 (1989).
[61]G. Armand, D. Gorse, J. Lapujoulade, and J. R. Manson, Europhys. Lett. **3**, 1113 (1987).
[62]G. Armand and P. Zeppenfeld, Phys. Rev. B **40**, 5936 (1989).
[63]H. Dürr, R. Schneider, and Th. Fauster, Phys. Rev. B **43**, 12 187 (1991).
[64]A. P. Baddorf and E. W. Plummer, Phys. Rev. Lett. **66**, 2770 (1991).
[65]C. J. Martin and D. A. O'Connor, J. Phys. C **10**, 3521 (1977).
[66]F. A. Lindemann, Z. Phys. **14**, 609 (1910).
[67]J. M. Ziman, *Principles of the Theory of Solids* (Cambridge University Press, Cambridge, England, 1964).
[68]M. O. Robbins, G. S. Grest, and K. Kremer, Phys. Rev. B **42**, 5579 (1990).
[69]J. Merikoski and J. Timonen (private communication).
[70]J. Henderson and L. Yang, Trans. Metall. Soc. AIME **221**, 72 (1961); L. Yang, S. Kado, and G. Derge, *ibid.* **212**, 628 (1956).
[71]J. W. M. Frenken, J. P. Toennies, and Ch. Wöll, Phys. Rev. Lett. **60**, 1727 (1988).
[72]J. J. Métois and J. C. Heyraud, J. Phys. (Paris) **50**, 3175 (1989).
[73]S. Iarlori, P. Carnevali, F. Ercolessi, and E. Tosatti, Surf. Sci. **211/212**, 55 (1989).

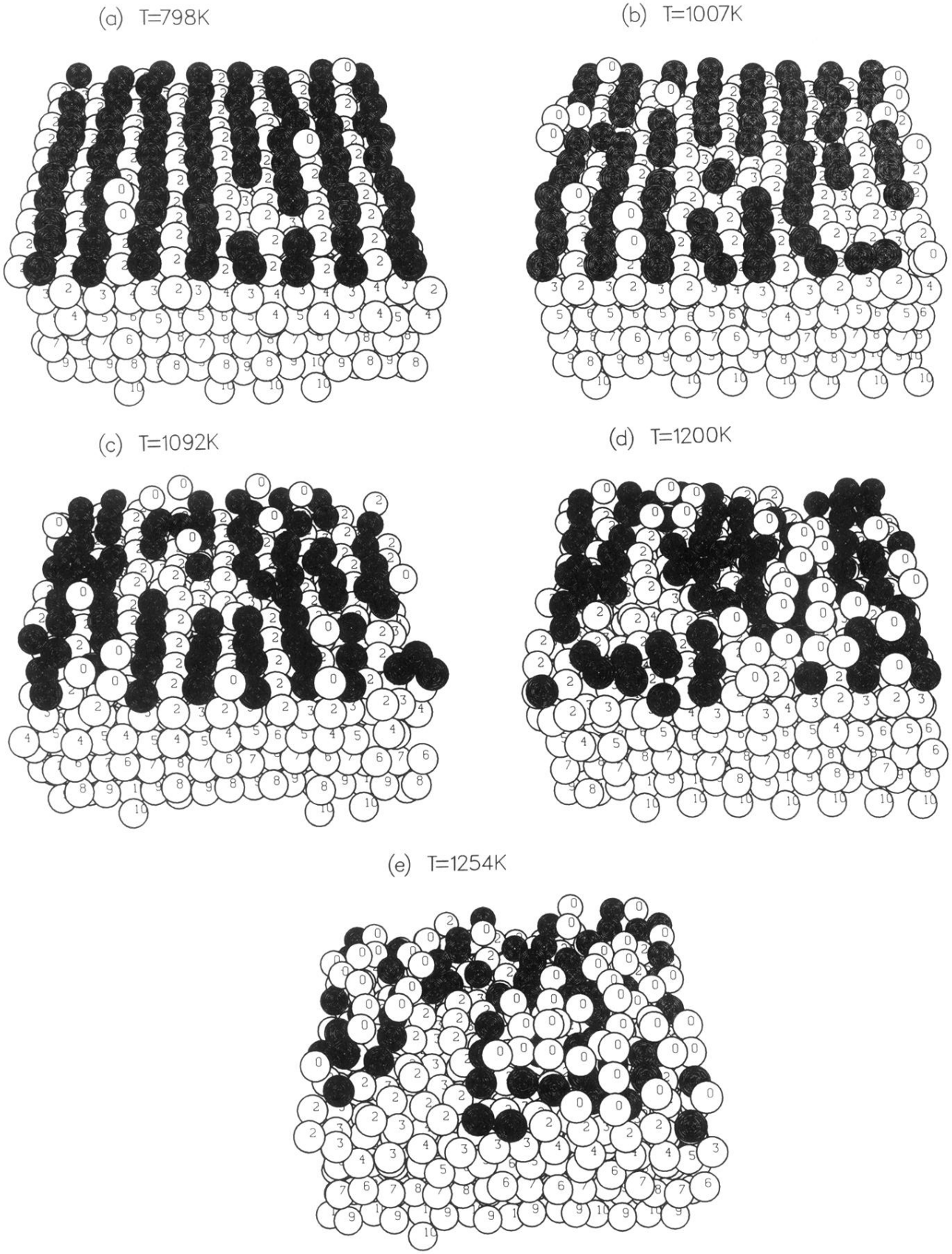

FIG. 16. Snapshots of configurations of (110) at (a) 798 K, (b) 1007 K, (c) 1092 K, (d) 1200 K, and (e) 1254 K. The numbers denote the crystal layers. The black atoms belong to the first crystal layer.